Journal of Applied Physics

RESEARCH ARTICLE | MARCH 26 2025

Engineering strong magnon–phonon coupling in single CoFe nanomagnets

Special Collection: Phonon-Magnon Interactions: From Fundamentals to Device Physics

Sujung Kim ; Becker Sharif ; Scott Dhuey; Thomas David Yuzvinsky ; Weigang Yang ; David Lederman ; Holger Schmidt

J. Appl. Phys. 137, 123904 (2025)
https://doi.org/10.1063/5.0254081

AIP Publishing

Journal of Applied Physics ARTICLE pubs.aip.org/aip/jap

Engineering strong magnon–phonon coupling in single CoFe nanomagnets

Cite as: J. Appl. Phys. **137**, 123904 (2025); doi: 10.1063/5.0254081
Submitted: 20 December 2024 · Accepted: 3 March 2025 ·
Published Online: 26 March 2025

Sujung Kim,[1,a)] Becker Sharif,[2] Scott Dhuey,[3] Thomas David Yuzvinsky,[1] Weigang Yang,[1] David Lederman,[2] and Holger Schmidt[1]

AFFILIATIONS

[1]Department of Electrical and Computer Engineering, University of California Santa Cruz, 1156 High Street, Santa Cruz, California 95064, USA
[2]Department of Physics, University of California Santa Cruz, 1156 High Street, Santa Cruz, California 95064, USA
[3]Molecular Foundry, University of California Berkeley, 67 Cyclotron Road, Berkeley, California 94720, USA

Note: This paper is part of the Special Topic, Phonon-Magnon Interactions: From Fundamentals to Device Physics.
[a)]**Author to whom correspondence should be addressed:** sujungkim@ucsc.edu

ABSTRACT

Hybrid magnonic systems are promising platforms for quantum technologies, leveraging coherent coupling between magnons and phonons. Here, we demonstrate strong magnon–phonon coupling in CoFe nanomagnets, a material with high magnetostriction. Using time-resolved magneto-optical Kerr effect spectroscopy, we demonstrate strong coupling between magnonic and phononic modes in both polycrystalline and single-crystalline CoFe nanomagnets. Our findings reveal strong coupling with cooperativity values of $C = 20.04$ for a polycrystalline CoFe nanomagnet and $C = 37.94$ for a single-crystalline CoFe nanomagnet. The enhanced coupling strength in the single-crystalline CoFe nanomagnet is attributed to the higher magnetostriction in CoFe systems and lower intrinsic magnetic damping. This work highlights the critical role of material properties and crystalline structures in optimizing hybrid magnon–phonon systems for miniaturized quantum applications.

INTRODUCTION

In recent years, hybrid quantum systems have attracted significant interest for their potential to explore fundamental quantum phenomena and advance quantum technologies.[1–29] Among these, hybrid magnonics—systems that couple magnons, the quanta of spin waves in magnetic materials, to other quantum entities such as photons, phonons, and superconducting qubits—have emerged as a promising platform for developing quantum information technologies.[2–6,8–11,13–20,22,24–30] This versatility positions magnons as essential components for coherent information transfer and quantum sensing across disparate quantum systems.

Within the realm of hybrid magnonics, the coupling between magnons and phonons (quantized lattice vibrations) has gained notable attention.[3–5,11,14,15,19,20,22,24,25] Magnon–phonon interactions enable the exchange of energy and information between spin and mechanical subsystems, opening the door to new possibilities in quantum communication and control. These interactions arise in magnetic materials due to magnetoelastic coupling, where changes in magnetization deform the lattice and vice versa. Understanding, controlling, and optimizing the dynamics of magnon–phonon coupling is essential for the development of coherent hybrid systems. Strong coupling between magnons and phonons has already been demonstrated in materials such as nickel (Ni),[25] iron gallium (FeGa),[20] and yttrium iron garnet (YIG).[31]

In this study, we focus on strongly increased magnon–phonon coupling in the CoFe material system. It has previously been reported that $Co_{25}Fe_{75}$ exhibits low magnetic damping[33] and $Co_{66}Fe_{34}$ exhibits a high magnetostriction coefficient of 260 ± 10 ppm.[32] Since both low magnetic damping and high magnetostriction coefficient are critical to maximize strong coupling of the magnon–phonon dynamics, $Co_{50}Fe_{50}$ (CoFe) was chosen as a representative CoFe system that balances between both of these requirements. Leveraging both properties, we have

optimized the cooperativity in a single-crystal CoFe nanomagnet. Maximizing these coherent effects in this technologically relevant material system can be leveraged for the development of future hybrid quantum systems that take advantage of the strong coupling properties of magnons and phonons on the nanoscale for quantum information processing and sensing.

STRONG COUPLING IN A POLYCRYSTALLINE CoFe NANOMAGNET

In order to assess the impact of increased magnetostriction, we first consider polycrystalline CoFe nanomagnets that can be fabricated with a simple, conventional lift-off process, analogous to the previously studied nickel samples. Square-shaped polycrystalline CoFe nanomagnets (here after, p-CoFe NMs) of dimensions of $210 \times 210 \times 30\,\text{nm}^3$ were patterned on silicon wafers by e-beam lithography. Specifically, 30 nm of $Co_{50}Fe_{50}$ was deposited via e-beam evaporation onto a patterned PMMA layer, followed by lift-off of the metal and e-beam PMMA layers [see Fig. 1(a) for an SEM image].

The magnetic and phononic responses of the fabricated p-CoFe NMs were measured using a time-resolved magneto-optic Kerr effect (TR-MOKE) technique with balanced photodetectors (BPD) as previously described.[25,34] Briefly, two-color pump–probe laser pulses are used where 800 nm pulsed laser beams are generated by a Ti:Sapphire laser (Coherent Mira 900-F) and split into two beam paths at the laser outlet. The stronger beam is directed into a second-harmonic generator (SHG) to create the pump beam at 400 nm, which is focused onto the magnetic sample plane to initiate magnetization dynamics ($t = 0$). On the other hand, the weaker beam passes a motorized delay stage to add the time delay ($t = \Delta t$) with respect to the pump beam. Upon reflection from the magnetic sample plane, the probe beam undergoes Kerr rotation depending on the magnetization state of the nanomagnet. The probe beam passes through a second polarizer (analyzer) and is split onto two balanced photodetectors that detect the horizontal and vertical polarization components of the probe beam, respectively. The sum of these signals represents the sample reflectivity, which reveals mechanical vibrations (hereafter, phononic channel), and the difference corresponds to the polarization rotation caused by the magneto-optic Kerr effect (hereafter, magnonic channel). Meanwhile, the pump beam is spectrally filtered out after reflection from the sample plane to selectively collect information for a change in polarization from the probe beam.

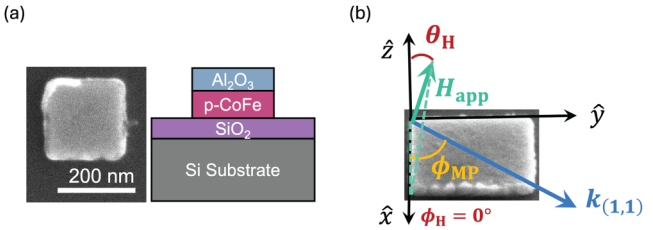

FIG. 1. (a) Scanning electron microscope (SEM) image of a nanomagnet ($210 \times 210 \times 30\,\text{nm}^3$) fabricated using electron-beam lithography. (b) Geometry of H_{app} and $k_{(1,1)}$ with respect to the x, y, z coordinate system superimposed on an SEM image of a p-CoFe nanomagnet.

The externally applied magnetic field was varied ($3\,\text{kOe} \leq H_{app} \leq 6\,\text{kOe}$) with the magnetic field applied parallel to one of the edges of the p-CoFe NM ($\phi_H = 0°$) at $\theta_H = 30°$ [Fig. 1(b)]. Additionally, the magnetic response of an unpatterned polycrystalline CoFe thin film (here after, p-CoFe thin film, thickness 30 nm) was measured for comparison with the magnetic dynamics of the p-CoFe NM.

The optically obtained frequency response of magnonic dynamics of the p-CoFe thin film is shown in Fig. 2(a). The experimentally taken magnonic frequency was fit to the Kittel mode as calculated by solving the Landau–Lifshitz–Gilbert equation (LLG) equation given by

$$\frac{d}{dt}\vec{\boldsymbol{m}}(t) = -\gamma[\vec{\boldsymbol{m}}(t) \times \vec{\boldsymbol{H}}_{\text{eff}}(t)] + \frac{\alpha}{M_S}\left(\vec{\boldsymbol{m}}(t) \times \frac{d}{dt}\vec{\boldsymbol{m}}(t)\right), \tag{1}$$

where the direction of magnetization $\vec{\boldsymbol{m}}(t) = \frac{\vec{\boldsymbol{m}}}{M}$, γ is the gyromagnetic ratio, and α is the Gilbert damping parameter. $\vec{\boldsymbol{H}}_{\text{eff}}$ is the effective magnetic field that consists of the sum of all magnetic fields that affects the magnetization dynamics. $\vec{\boldsymbol{H}}_{\text{eff}}$ is expressed in terms of the Gibbs free energy G [energy density normalized to M_S (Ref. 35)], given by

$$\begin{aligned} \vec{\boldsymbol{H}}_{\text{eff}} &= -\vec{\nabla}_{\mathbf{m}} G, \\ G &= G_{\text{Zeeman}} + G_{\text{Shape}}, \end{aligned} \tag{2}$$

where $G_{\text{Zeeman}} = -\vec{\boldsymbol{H}}_{\text{app}} \cdot \vec{\boldsymbol{m}}$, $G_{\text{Shape}} = \frac{1}{2M_S} N_z (M_S m_z)^2$ with $N_z = 4\pi$, which is the demagnetization constant for thin films. We take the coordinate transformation from the Cartesian coordinate system to the local (1, 2, 3) coordinate system aligned with the equilibrium direction of magnetization (see Fig. S1 in the supplementary material) to better represent the precession dynamics. We also take a small angle approximation near equilibrium and $\alpha = 0$ for simplicity. A detailed derivation can be found in the supplementary material (S1). Therefore, the total Gibbs free energy of the polycrystalline thin film in Eq. (2) at equilibrium is generalized by

$$G = -H_{\text{app}}\cos(\theta_H - \theta_M) + 2\pi M_S(\cos\theta_M)^2, \tag{3}$$

where θ_H is the polar angle of the externally applied magnetic field and θ_M is the polar angle of the magnetization vector.

Solving Eq. (1) by substituting Eq. (3), the frequency response is generalized by

$$\left(\frac{\omega_M}{\gamma}\right)^2 = (G_{22} - G_3)(G_{11} - G_3) - G_{12}^2, \tag{4}$$

where $G_{ij} = \frac{\partial^2 G}{\partial m_i \partial m_j}\Big|_{\vec{\boldsymbol{m}}=\vec{\boldsymbol{m}}_0}$, $G_{11} = 4\pi M_s(\sin\theta_M)^2$, $G_{12} = G_{21} = 0$, $G_{22} = 0$, and $G_3 = -H_{\text{app}}\cos(\theta_H - \theta_M) + 4\pi M_s(\cos\theta_M)^2$. With this given, the Kittel frequency for a polycrystalline thin film follows

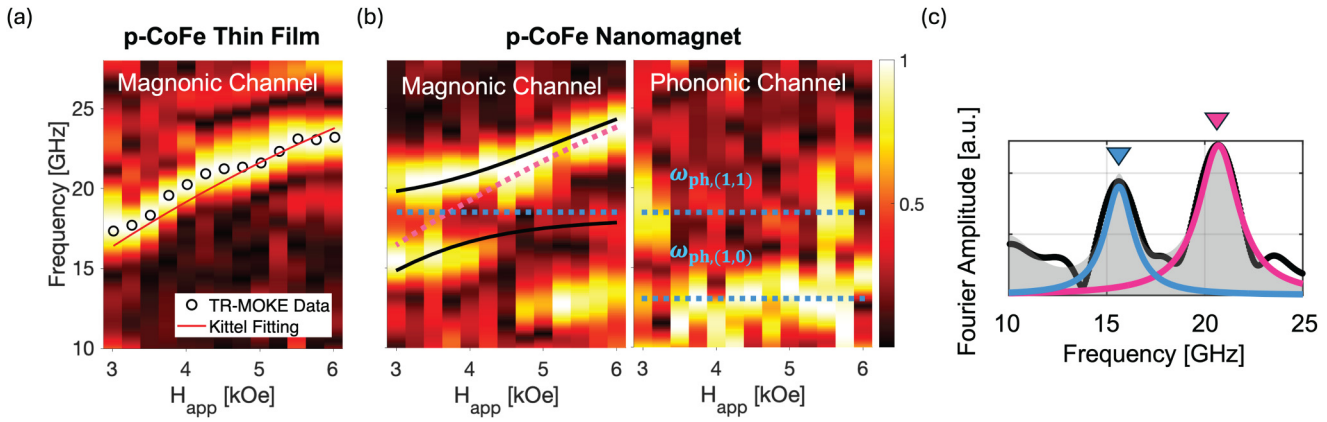

FIG. 2. (a) and (b) Fourier-transformed TR-MOKE data. (a) The frequency response of magnonic dynamics of the p-CoFe thin film. Black circles represent the experimentally taken data points, and the red line is the fit to the Kittel mode for the p-CoFe thin film. (b) The frequency response in the magnonic (left) and phononic (right) channels of the p-CoFe NM. The pink (blue) dotted lines indicate the magnonic (phononic) responses without the presence of magnon–phonon coupling, and the black solid line represents the fit to the coupled magnon–phonon dynamics, showing good agreement with the experimentally obtained data. (c) Mode splitting of two frequencies at the (1, 1) crossing (at $H_{app} = 4.00$ kOe), marked with two arrows. Fitting to Lorentzians was used for the three frequencies responsible for the (1, 0) and (1, 1) crossings. The two frequencies fitted for the (1, 1) crossing are shown with blue and pink lines with their peaks marked with arrows.

$$\omega_M = \gamma\sqrt{[H_{app}\cos(\theta_H-\theta_M)-4\pi M_S\cos(2\theta_M)][H_{app}\cos(\theta_H-\theta_M)-4\pi M_S(\cos\theta_M)^2]}. \quad (5)$$

Fitting to Eq. (5) for the p-CoFe thin film data gave $M_S = 1620\,\text{emu/cm}^3$ and $\gamma = 1.76 \times 10^7$ rad/Oe s. Next, the magnonic and phononic responses were obtained in a p-CoFe NM, using the same TR-MOKE technique [Fig. 2(b)]. The magnonic mode without considering the magnon–phonon coupling was taken from the Kittel mode fitted in the CoFe thin film as shown in Fig. 2(a), which is plotted with the pink dotted line.

Similarly, the phononic mode without the presence of magnon–phonon coupling is presented with the blue dotted lines in Fig. 2(b), which was fit to the equation[25]

$$\omega_{ph} = \frac{(2\lambda+3\mu)k^2}{2\rho}. \quad (6)$$

In this equation, $C_{11} = 2\mu + \lambda$, $C_{12} = \lambda$, $C_{44} = \mu$, and C_{ij} are the elements of the stiffness tensor, where Lamé's first parameter, $\lambda = \frac{E\nu}{(1+\nu)(1-2\nu)}$, and Lamé's second parameter, $\mu = \frac{E}{2(1+\nu)}$, are expressed in terms of Young's modulus E and Poisson's ratio ν. The in-plane wavevector components of the phononic mode are defined as $k_{x,y} = \frac{n_{x,y}\pi}{l_{x,y}}$, where $n_{x,y}$ are indices ($n_{x,y} \geq 0$, integers) and $l_{x,y}$ represents the dimensions of the nanoelement along the x- and y-directions. Using this notation, the phononic mode is characterized by the indices (n_x, n_y).

Noticeable changes in magnetic response were observed in the magnonic channel in the p-CoFe NM compared to the p-CoFe thin film. Particularly, a clear anti-crossing was observed at the frequency where the uncoupled magnonic and phononic modes would naturally overlap. To account for the coupled dynamics of magnon–phonon interaction, the two observed frequencies near the phononic (1, 1) crossing shown in the magnonic channel were fit to the coupled equation[25,36]

$$(\omega^2-\omega_{ph}^2)[(\omega^2-\omega_M^2)(\omega^2-\omega_{ph}^2)-\omega_C^4] = 0, \quad (7)$$

where

$$\omega_C^4 = \frac{\gamma M_S}{\rho}(\omega_1 C_2 + \omega_2 C_1)k^2,$$

$$\omega_1 = \gamma(G_{11} - G_3),$$

$$\omega_2 = \gamma(-G_3),$$

$$C_1 = b_1^2(\cos^2\phi_k w_1^2 + \sin^2\phi_k w_3^2) + \frac{3}{4}b_1 b_2 \sin 2\phi_k w_2(w_1+w_3) + \frac{1}{2}b_2^2 w_2^2,$$

$$C_2 = b_1^2 w_4^2 + 2b_2^2 w_5^2,$$

$$b_1 = b_2 = -\frac{3\lambda_S C_{44}}{M_S},$$

$$w_1 = \sin 2\theta_M \cos^2\phi_{MP},$$

$$w_2 = \sin 2\theta_M \sin 2\phi_{MP},$$

$$w_3 = \sin 2\theta_M \sin^2 \phi_{MP},$$

$$w_4 = \sin \theta_M \sin 2\phi_{MP},$$

$$w_5 = \sin \theta_M \cos 2\phi_{MP}.$$

Here, b_1 represents the magnetoelastic constant for compressive/tensile stress and b_2 represents the magnetoelastic constant for shear stress. ϕ_k is the azimuthal angle of the phononic mode with respect to the x axis and ϕ_{MP} is the azimuthal angle between magnetization and phononic mode. For the polycrystalline sample, we assumed $b_1 = b_2$ was approximated for the polycrystalline NM due to the lack of crystalline anisotropy, and for the single-crystalline sample, for simplicity, we used $b_1 = b_2 = b_{eff}$ to calculate $\lambda_{S,eff}$, where $b_{eff} = -\frac{3\lambda_{S,eff} C_{44}}{M_S}$. The three solutions to the equation above are $\omega = \omega_{ph}$ and $(\omega^2 - \omega_M^2)(\omega^2 - \omega_{ph}^2) - \omega_C^4 = 0$, in which the latter solutions account for the two frequencies of the coupled magnon–phonon system.

The fitting of the p-CoFe NM was performed using the solutions of Eq. (7), assuming $\rho = 8190\,kg/m^3$ and $\nu = 0.29$ for CoFe, the dimensions of the p-CoFe NM were $208 \times 208\,nm^2$, and using the previously fitted parameters $M_S = 1620\,emu/cm^3$ and $\gamma = 1.76 \times 10^7\,rad/Oe\,s$ for the p-CoFe thin film. The resulting coupled modes were plotted with the solid black solid line in Fig. 2(b), for phononic (1, 1) crossing, giving $E = 217\,GPa$ and $\lambda_S = 247 \times 10^{-6}$. This large magnetostriction coefficient in the CoFe material system is in reasonable agreement with the previously reported values[32] and confirms CoFe's suitability as a high magnetostriction material for magnon–phonon coupled systems.

The two coupled modes at the (1, 1) crossing were fit to Lorentzian line shapes to account for the damped sinusoidal character of the optical TR-MOKE measurement in the time domain taken [Fig. 2(c), pink and blue lines]. As shown in Fig. 2(c), the two frequencies are clearly separated at the (1, 1) crossing, which is the hallmark of strong coupling. Furthermore, the minimum frequency splitting (Δf_{min}) of 5.08 GHz was taken at the minimum frequency fitting at $H_{app} = 4.00\,kOe$ [subtraction of two black lines in Fig. 2(c)], which is a 3.6 times larger splitting than was previously observed on a single Ni nanomagnet ($\Delta f_{min,Ni} = 1.41\,GHz$, (2, 0) crossing at $\phi_H = 45°$).[25]

The quantitative figure of merit of coupling of two quanta is cooperativity defined as $C = \frac{\Gamma_C^2}{\kappa_M \kappa_P}$. The parameter $\Gamma_C = \Delta f_{min}/2$ was taken from the minimum frequency splitting measurement described above in the p-CoFe NM, and $\kappa_M = f_M \alpha_{eff,M}$ was taken from the uncoupled magnonic dynamics in the p-CoFe thin film to accommodate the uncoupled magnonic damping as well as the fact that $\alpha_{eff,M}$ depends on H_{app}. Thus, $\alpha_{eff,M}$ was extracted from the applied field where Δf_{min} was taken ($H_{app} = 4.00\,kOe$) from the p-CoFe thin film data. For phonons, $\kappa_P = f_P \alpha_{eff,P}$ was taken from the phononic channel in the CoFe NM at $H_{app} = 6.00\,kOe$ away from the coupled region of H_{app}. For the (1, 1) crossing, we find $\alpha_{eff,M} = 0.0562$ at $f_M = 20.69\,GHz$, yielding an intrinsic loss rate for magnon $\kappa_M = 1.11\,GHz$, and $\alpha_{eff,P} = 0.0202$ at $f_P = 14.56\,GHz$, giving the intrinsic loss rate for phonon $\kappa_P = 0.29\,GHz$. With $\Gamma_C = 2.54\,GHz$, cooperativity was calculated to be $C = 20.04$, demonstrating enlarged strong coupling in the polycrystalline CoFe system, despite the 2.5 times smaller volume of the p-CoFe nanomagnet in this study compared to the previously reported analogous system with a Ni NM.[25] As discussed, this cooperativity enhancement is mainly due to the larger magnetostriction coefficient in CoFe.

STRONG COUPLING IN A SINGLE-CRYSTAL CoFe NANOMAGNET

However, the decay rate for the magnons (effective Gilbert damping) in the p-CoFe NM was higher than in the Ni NM due to the stronger spin–orbit coupling (SOC) in the CoFe material system, which is also responsible for the high magnetostriction coefficient. To overcome this trade-off and maximize magnon–phonon coupling, it is desirable to use materials with a high magnetostriction coefficient, and at the same time, with a low magnetic damping parameter. To this end, we turn to higher quality single-crystalline CoFe materials (hereafter, s-CoFe NM) that require a completely different nanomagnet fabrication process.

FABRICATION PROCESS FOR s-CoFe NM

The patterning process developed for making s-CoFe nanomagnets is shown in Fig. 3(a). First, a MgO [001] substrate was thermally annealed and a thin layer of MgO was deposited using pulsed laser deposition (PLD). The substrate was then transferred to an RF-sputtering chamber without breaking vacuum, and $Co_{50}Fe_{50}$ was sputtered at room temperature, followed by annealing (500 °C for 30 min) and cooling (400 °C for 1h) steps. Finally, the sample was transferred back to the PLD chamber to deposit a thin MgO capping layer (1.4 nm). The crystalline structure of the film was then characterized before the patterning process (data shown in supplementary material, S2). Next, a 30 nm copper sacrificial layer and a hydrogen silsesquioxane (HSQ) resist layer were deposited on top of the CoFe film. The HSQ layer was patterned by electron-beam lithography to define a hard mask for the ion-beam etching (IBE) process. IBE was performed at a beam voltage of 400 V, beam current of 30 mA, and a stage angle of 95° (5° off from the surface normal direction), for 5 min 30 s in an 11 SCCM Ar environment. The HSQ hard mask was removed by etching copper in a citric acid-based Cu wet etchant (Copper Etchant 49-1, Transene Company, Inc.) in a magnetic stirrer at 25 °C at 300 rpm for 15 min. The sample was then immediately soaked in a de-ionized (DI) water bath followed by rinsing it with DI water using a syringe to prevent HSQ hard mask residues from adhering back to the s-CoFe NMs. The sample was rinsed in DI water again and then dried with N_2 gas.

After the patterning process, the magnetic properties of the films were characterized to determine if the patterning process was CoFe-compatible. Their characterization was done by performing TR-MOKE on the s-CoFe film both before and after the patterning process (data shown in supplementary material, S3). The result shows that the magnetization character of s-CoFe was preserved throughout the entire patterning process, demonstrating that the patterning process used for the s-CoFe NM using the Cu sacrificial

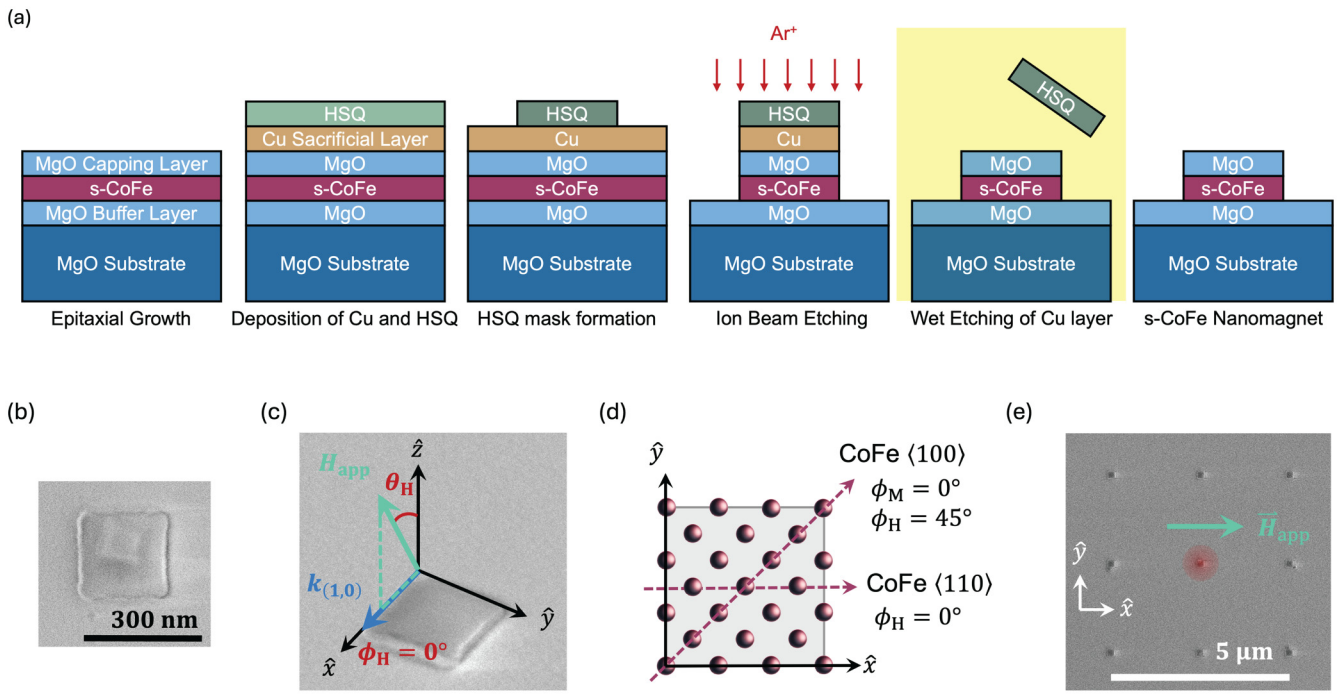

FIG. 3. (a) Fabrication process flow (from left to right) of the s-CoFe NM. (b) SEM images of one of the single-crystalline CoFe nanomagnets fabricated using the process described in (a). The scale bar is 300 nm. (c) Geometry of H_{app} and $k_{(1,0)}$ with respect to the x, y, z coordinate system superimposed on a tilted SEM image of the nanomagnet patterned at different sizes (340 nm). (d) Crystalline orientation of the s-CoFe NM (represented by pink spheres) with respect to the shape of the nanomagnet (outlining gray square). The edges of the nanomagnet align with the CoFe⟨110⟩ orientation. ϕ_H aligns with the x axis, whereas ϕ_M aligns along the CoFe⟨100⟩ orientation. (e) SEM image showing excitation schematics. The red circle around the nanomagnet center represents the area of probe beam illumination. Multiple isolated nanomagnets are patterned far enough apart to ensure isolated measurements. H_{app} is applied along the $\hat{x}$ axis parallel to the edge of the nanomagnet (CoFe⟨110⟩ orientation).

layer with the citric acid-based Cu etchant was CoFe-compatible. This patterning process can be extended to various magnetic material systems with a Cu sacrificial layer, because the citric acid-based etchant is Cu-selective.

The coupled magnon–phonon dynamics of a single s-CoFe NM ($210 \times 210 \times 10.8\,\text{nm}^3$) were then measured using the same TR-MOKE technique as described earlier. The nanomagnet dynamics were then compared to those of a large ($5 \times 5\,\mu\text{m}^2$) film-like unpatterned area that exhibits the intrinsic magnonic dynamics of the material [see Fig. 4(a)].

The magnetic field was applied between $0.75\,\text{kOe} \leq H_{app} \leq 3.5\,\text{kOe}$, $\theta_H = 30°$, and $\phi_H = 0°$ ($H_{app,in-plane} \parallel \langle 110 \rangle_{CoFe}$) [Figs. 3(d) and 3(e)], and the resulting optical responses in the frequency domain are demonstrated in Figs. 4(a) and 4(b). In the uncoupled magnon response, a single frequency at each applied magnetic field was observed [Fig. 4(a), scatterplot] and fitted to the Kittel mode [Fig. 4(a), solid line] calculated using Eq. (4) by substituting the total energy including magnetocrystalline energy and uniaxial energy for the single-crystalline thin film. Here, the total Gibbs free energy becomes

$$G_{total} = G_{Zeeman} + G_{Shape} + G_{MagCrys} + G_{Uni}, \tag{8}$$

where $G_{MagCrys} = \frac{K_1}{M_S}[(\alpha_1\alpha_2)^2 + (\alpha_2\alpha_3)^2 + (\alpha_3\alpha_1)^2]$ is the magnetocrystalline anisotropy energy and $G_{Uni} = -\frac{K_U}{M_S}\alpha_3^2$ is the out-of-plane uniaxial anisotropy, where α_1, α_2, and α_3 are direction cosines. Unlike for the case of the polycrystalline film, the azimuthal angles of $H_{app}(\phi_H)$ and the azimuthal angle of magnetization (ϕ_M) were not assumed to align in the single-crystalline film due to in-plane anisotropy in the single-crystalline film. Assuming $\rho = 8190\,\text{kg/m}^3$ and $\nu = 0.29$ for CoFe, the fitting returned $\gamma = 1.80 \times 10^7$ rad/Oe s, and $M_S = 1961\,\text{emu/cm}^3$.

The frequency response of the coupled magnonic and phononic dynamics was experimentally measured and plotted in Fig. 4(b). The uncoupled magnonic mode is plotted as a pink dotted line, using the Kittel fitting from the s-CoFe thin film. Likewise, the phononic mode without considering coupling is plotted as the blue dotted line, which is fitted to Eq. (6). Similar to the coupled magnon–phonon dynamics observed in the p-CoFe NM, the anticrossing hallmark of strong coupling was observed in the s-CoFe NM. This anticrossing behavior of the coupled dynamics was fitted to Eq. (7) with dimensions of the s-CoFe NM of $210 \times 210\,\text{nm}^2$, where the total energy density (G_{total}) was altered to reflect the free energy density of the single-crystalline film and plotted in Fig. 4(b) in solid black lines. In the calculation, $\phi_{MP} = 0°$ for $(1, 0)$ phonon crossing.

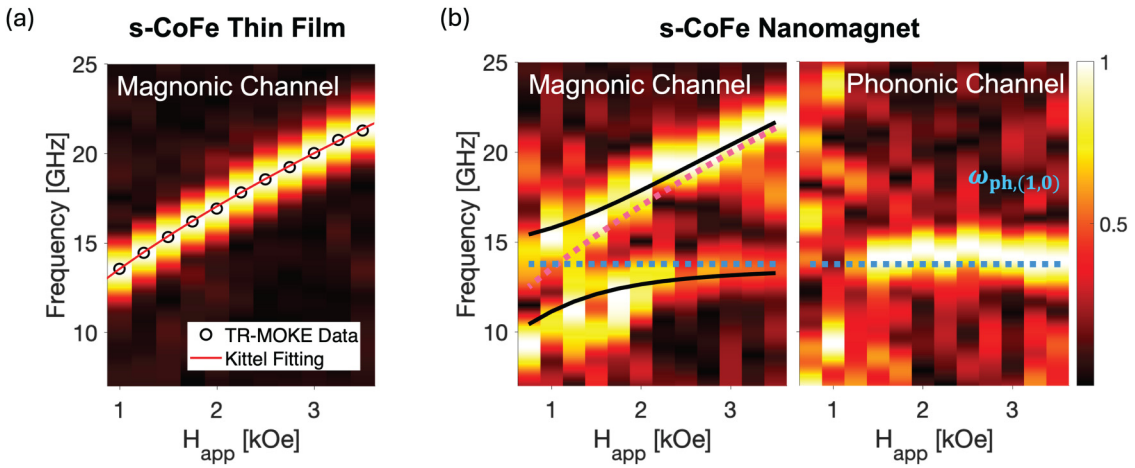

FIG. 4. Fourier transformed TR-MOKE data in the frequency domain. (a) The frequency response of magnonic dynamics of the s-CoFe thin film at $\theta_H = 30°$ and $\phi_H = 0°$. Black circles represent the experimentally taken data points, and the red line is the fit to the Kittel mode for the s-CoFe thin film. (b) The magnonic (left) and phononic (right) frequency responses of the s-CoFe NM. The pink (blue) dotted line indicates the magnonic (phononic) mode without the presence of magnon–phonon coupling, and the black solid line represents the fit to the coupled magnon–phonon dynamics showing excellent agreement with the experimentally obtained data.

The corresponding fitting provided parameters of $E = 256\,\text{GPa}$, $\lambda_{S,\text{eff}} = 175 \times 10^{-6}$, and $b_{\text{eff}} = -26.55 \times 10^{-4}\,\text{Oe}$.

The two frequencies at anticrossing for the (1, 0) phonon mode were fitted using Lorentzians to account for the damped sinusoidal time trace, as shown in Fig. 5(a) in pink and blue lines with their peak frequency locations indicated with arrows. The difference in the two frequencies (mode splitting) is plotted in Fig. 5(b), showing good agreement with the fitting. Furthermore,

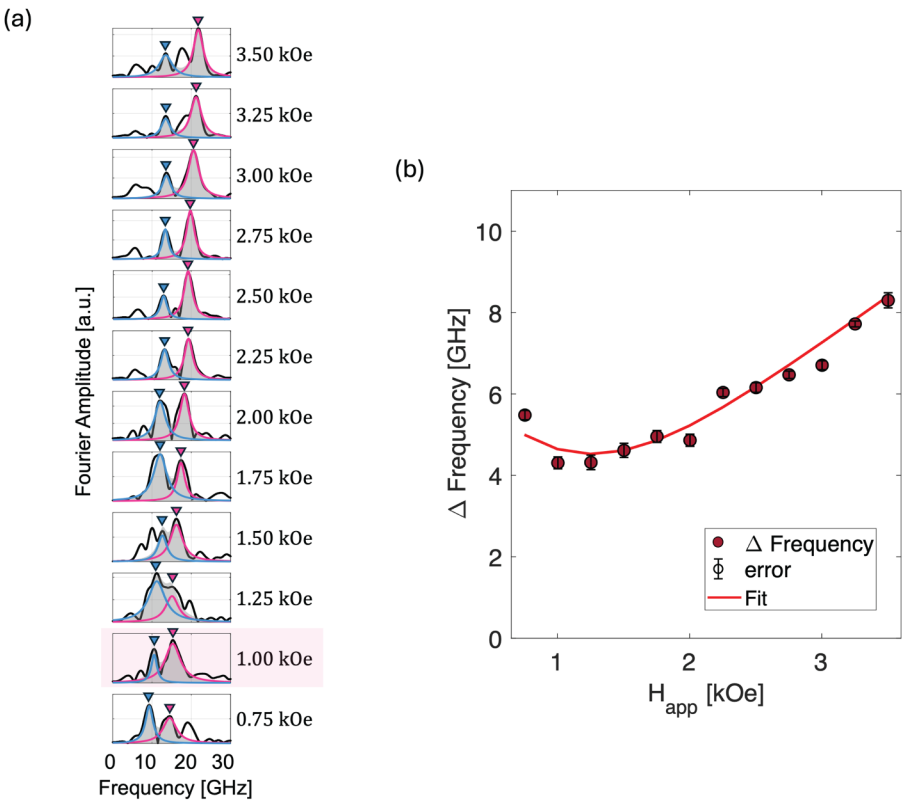

FIG. 5. (a) Fourier transformed TR-MOKE data in the frequency domain with $0.75\,\text{kOe} \leq H_{app} \leq 3.5\,\text{kOe}$. The Lorentzian distribution of the two main frequencies responsible for magnon–phonon coupling is plotted with blue and pink lines. (b) The frequency splitting Δf of two corresponding peaks vs H_{app}. The TR-MOKE data are plotted as symbols and the fitting is plotted with a red solid line. Error bars represent the uncertainties calculated using the covariance function.

TABLE I. Summary of the coupling strength, loss rate, and cooperativity among Ni NM, p-CoFe NM, and s-CoFe NM.

Material	Crossing	Γ_C(GHz)	κ_M(GHz)	κ_P(GHz)	C
Ni	(2, 0), 45°	0.71	0.65	0.47	1.65
p-CoFe	(1, 1) 0°	2.54	1.11	0.29	20.04
s-CoFe	(1, 0), 0°	2.15	0.41	0.29	37.94

$\Delta f_{min} = 4.31$ GHz was observed where the magnonic and phononic modes cross at $H_{app} = 1.00$ kOe [Fig. 5(a), highlighted] which is three times larger than the splitting found in a single Ni NM,[25] indicating significantly larger coherent coupling.

To quantify the strength of the magnon–phonon coupling, cooperativity was calculated following the same analysis done for the p-CoFe NM. For the (1, 0) crossing, $\alpha_{eff,M} = 0.0306$ at $f_M = 13.55$ GHz, giving an intrinsic loss rate for the magnon of $\kappa_M = 0.41$ GHz, and $\alpha_{eff,P} = 0.0206$ at $f_P = 14.29$ GHz, yielding an intrinsic loss rate for phonons of $\kappa_P = 0.29$ GHz. With $\Gamma_C = 2.15$ GHz, cooperativity was calculated as $C = 37.94$ (Table I), again, demonstrating further enhanced strong coupling in the single s-CoFe NM system. Compared with p-CoFe, the cooperativity is almost two times larger, despite a 2.62 times smaller volume compared. Likewise, compared to polycrystalline nickel, cooperativity is 23 times larger, despite a 6.6 times smaller nanomagnet volume. This maximization was achieved by introducing a single-crystalline nanomagnet that contributed a lower magnon loss rate ($\kappa_{M,s-CoFe} = 0.0306$ GHz) compared to the p-CoFe NM ($\kappa_{M,p-CoFe} = 0.0537$ GHz). It is worth noting that $\kappa_{P,s-CoFe}$ was not improved compared to $\kappa_{P,p-CoFe}$, due to the pinning of the s-CoFe NM on the surface of the substrate, similar to the p-CoFe NM.

Given that the coupling strength Γ_C depends on the number of spins, assuming that the spins are collectively precessing at a uniform mode,[8,27,37] the coupling strength of a single Bohr magneton and cooperativity per unit volume were also calculated as a figure of merit for the different material systems. The coupling strength per Bohr magneton, Γ_0 is given by $\Gamma_0 = \Gamma_C/\sqrt{N}$, where $N = M_S V/(\gamma\hbar/2)$ is the total number of spins, V is the volume of the magnetic specimen, and $\hbar$ is the Planck constant. Table II summarizes the strength of coupling in different magnon–phonon hybrid systems, including a YIG sphere where magnon–photon coupling was studied with $C = 13,000$.[8]

TABLE II. Summary of coupling strength Γ_C, number of spins N, cooperativity C, coupling strength for a single Bohr magneton Γ_0, and cooperativity per unit volume C/V among the YIG sphere, Ni NM, p-CoFe NM, and s-CoFe NM. Note that the parameters for the YIG sphere were taken from magnon–photon coupling.[8]

Material	Γ_C(GHz)	N ($\times 10^7$)	C	Γ_0(Hz)	$C/V(\mu m^{-3})$
YIG	0.136	1.2×10^{10}	13, 000	0.38	0.001 589
Ni	0.71	6.35	1.65	88.5×10^3	505
p-CoFe	2.54	22.61	20.04	168.9×10^3	15, 440
s-CoFe	2.15	10.22	37.94	212.9×10^3	76, 709

By comparing Γ_0 between three nanomagnets of Ni NM, p-CoFe NM, and s-CoFe NM, the coupling strength for a single Bohr magneton for all Ni and CoFe were found to be in the same order ($\Gamma_{0,Ni} = 88.5$ kHz, $\Gamma_{0,p-CoFe} = 168.9$ kHz, $\Gamma_{0,s-CoFe} = 212.9$ kHz), but much larger in comparison to YIG ($\Gamma_{0,YIG} = 0.38$ Hz). To obtain a better comparison among the nanomagnets that accounts for their different sizes, we calculate the cooperativity per unit volume (C/V in μm^{-3}). C/V in the s-CoFe NM was found to be 4.97 times larger than in the p-CoFe NM, and 151.88 times larger than in the Ni NM. Compared to the YIG sphere, the C/V value was even 4.83×10^6 times higher due to the large magnetostriction coefficient and higher saturation magnetization in CoFe.

In summary, this study highlights the potential of single-crystalline CoFe as an attractive material system for implementing magnon–phonon hybrid quantum systems as effective platforms for miniaturized applications, emphasizing the critical role of material selection and crystallinity in achieving strong magnon–phonon coupling. The coupling strength of the proposed system could be further enhanced by optimizing the relative orientations of the nanomagnet and the applied field,[25] and by employing free-standing structures to unpin phononic vibrations from the substrate, thereby reducing the decay rate of the phononic mode.[38] CoFe nanomagnets emerge as promising candidates for rare-earth-free hybrid magnon–phonon systems, offering significant advantages for miniaturized quantum information processing and sensing applications.

SUPPLEMENTARY MATERIAL

See the supplementary material for the derivation of resonant frequency (S1), x-ray analysis (S2), and validation of the patterning process (S3).

ACKNOWLEDGMENTS

The authors thank Thomas Eugene Carver at the Stanford Nano Shared Facilities and Cassidy Berk for valuable discussions, and they acknowledge the W. M. Keck Center for Nanoscale Optofluidics at UC Santa Cruz. A part of this work was performed at the Stanford Nano Shared Facilities (SNSF) RRID:SCR_023230, supported by the National Science Foundation under Award No. ECCS-2026822. Work at the Molecular Foundry was supported by the Office of Science, Office of Basic Energy Sciences, of the U.S. Department of Energy under Contract No. DE-AC02-05CH11231.

AUTHOR DECLARATIONS

Conflict of Interest

The authors have no conflicts to disclose.

Author Contributions

Sujung Kim: Conceptualization (equal); Data curation (equal); Formal analysis (equal); Investigation (equal); Methodology (equal); Software (equal); Validation (equal); Visualization (equal); Writing – original draft (equal); Writing – review & editing (equal). **Becker Sharif:** Data curation (equal); Formal analysis (equal); Methodology

(equal). **Scott Dhuey:** Formal analysis (equal); Methodology (equal); Resources (equal). **Thomas David Yuzvinsky:** Data curation (equal); Formal analysis (equal); Methodology (equal); Writing – review & editing (equal). **Weigang Yang:** Methodology (equal). **David Lederman:** Data curation (equal); Formal analysis (equal); Methodology (equal); Resources (equal); Software (equal); Visualization (equal); Writing – review & editing (equal). **Holger Schmidt:** Conceptualization (equal); Data curation (equal); Formal analysis (equal); Funding acquisition (equal); Investigation (equal); Project administration (equal); Resources (equal); Supervision (equal); Validation (equal); Writing – review & editing (equal).

DATA AVAILABILITY

The data that support the findings of this study are available from the corresponding author upon reasonable request.

REFERENCES

[1]X. Zhou *et al.*, "Electron charge qubit with 0.1 millisecond coherence time," Nat. Phys. **20**, 116–122 (2024).
[2]J. Xu *et al.*, "Slow-wave hybrid magnonics," preprint http://arxiv.org/abs/2402.08872 (2024).
[3]B. Flebus *et al.*, "The 2024 magnonics roadmap," J. Phys.: Condens. Matter **36**, 363501 (2024).
[4]X. Zhang, "A review of common materials for hybrid quantum magnonics," Mater. Today Electron. **5**, 100044 (2023).
[5]K. Wang, K. Ren, Y. Hou, Y. Cheng, and G. Zhang, "Magnon–phonon coupling: From fundamental physics to applications," Phys. Chem. Chem. Phys. **25**, 21802–21815 (2023).
[6]A. H. Comstock *et al.*, "Hybrid magnonics in hybrid perovskite antiferromagnets," Nat. Commun. **14**, 1834 (2023).
[7]X.-B. Xu, W.-T. Wang, L.-Y. Sun, and C.-L. Zou, "Hybrid superconducting photonic-phononic chip for quantum information processing," Chip **1**, 100016 (2022).
[8]Y. Li *et al.*, "Coherent coupling of two remote magnonic resonators mediated by superconducting circuits," Phys. Rev. Lett. **128**, 047701 (2022).
[9]A. Kimel *et al.*, "The 2022 magneto-optics roadmap," J. Phys. D: Appl. Phys. **55**, 463003 (2022).
[10]J. Inman *et al.*, "Hybrid magnonics for short-wavelength spin waves facilitated by a magnetic heterostructure," Phys. Rev. Appl. **17**, 044034 (2022).
[11]A. V. Chumak *et al.*, "Advances in magnetics roadmap on spin-wave computing," IEEE Trans. Magn. **58**, 1–72 (2022).
[12]S. Abo *et al.*, "Hybrid photon–phonon blockade," Sci. Rep. **12**, 17655 (2022).
[13]Y. Xu, T. Yang, L. Lin, and J. Song, "Conventional and unconventional magnon blockades in a qubit-magnon hybrid quantum system," J. Opt. Soc. Am. B **38**, 876 (2021).
[14]P. Pirro, V. I. Vasyuchka, A. A. Serga, and B. Hillebrands, "Advances in coherent magnonics," Nat. Rev. Mater. **6**, 1114–1135 (2021).
[15]Y. Li, C. Zhao, W. Zhang, A. Hoffmann, and V. Novosad, "Advances in coherent coupling between magnons and acoustic phonons," APL Mater. **9**, 060902 (2021).
[16]D. D. Awschalom *et al.*, "Quantum engineering with hybrid magnonic systems and materials *(invited paper)*," IEEE Trans. Quantum Eng. **2**, 1–36 (2021).
[17]Y. Li *et al.*, "Hybrid magnonics: Physics, circuits, and applications for coherent information processing," J. Appl. Phys. **128**, 130902 (2020).
[18]P.-B. Li, Y. Zhou, W.-B. Gao, and F. Nori, "Enhancing spin-phonon and spin-spin interactions using linear resources in a hybrid quantum system," Phys. Rev. Lett. **125**, 153602 (2020).
[19]D. M. Juraschek, P. Narang, and N. A. Spaldin, "Phono-magnetic analogs to opto-magnetic effects," Phys. Rev. Res. **2**, 043035 (2020).
[20]F. Godejohann *et al.*, "Magnon polaron formed by selectively coupled coherent magnon and phonon modes of a surface patterned ferromagnet," Phys. Rev. B **102**, 144438 (2020).
[21]A. W. Elshaari, W. Pernice, K. Srinivasan, O. Benson, and V. Zwiller, "Hybrid integrated quantum photonic circuits," Nat. Photonics **14**, 285–298 (2020).
[22]D. Lachance-Quirion, Y. Tabuchi, A. Gloppe, K. Usami, and Y. Nakamura, "Hybrid quantum systems based on magnonics," Appl. Phys. Express **12**, 070101 (2019).
[23]A. A. Clerk, K. W. Lehnert, P. Bertet, J. R. Petta, and Y. Nakamura, "Hybrid quantum systems with circuit quantum electrodynamics," Nat. Phys. **16**, 257–267 (2020).
[24]A. Barman, S. Mondal, S. Sahoo, and A. De, "Magnetization dynamics of nanoscale magnetic materials: A perspective," J. Appl. Phys. **128**, 170901 (2020).
[25]C. Berk *et al.*, "Strongly coupled magnon–phonon dynamics in a single nanomagnet," Nat. Commun. **10**, 2652 (2019).
[26]X. Zhang, C.-L. Zou, L. Jiang, and H. X. Tang, "Cavity magnomechanics," Sci. Adv. **2**, e1501286 (2016).
[27]Y. Tabuchi *et al.*, "Hybridizing ferromagnetic magnons and microwave photons in the quantum limit," Phys. Rev. Lett. **113**, 083603 (2014).
[28]H. Huebl *et al.*, "High cooperativity in coupled microwave resonator ferrimagnetic insulator hybrids," Phys. Rev. Lett. **111**, 127003 (2013).
[29]G. Kurizki *et al.*, "Quantum technologies with hybrid systems," Proc. Natl. Acad. Sci. U.S.A. **112**, 3866–3873 (2015).
[30]X. Zhang, C.-L. Zou, L. Jiang, and H. X. Tang, "Strongly coupled magnons and cavity microwave photons," Phys. Rev. Lett. **113**, 156401 (2014).
[31]H. Man *et al.*, "Direct observation of magnon-phonon coupling in yttrium iron garnet," Phys. Rev. B **96**, 100406 (2017).
[32]D. Hunter *et al.*, "Giant magnetostriction in annealed $Co_{1-x}Fe_x$ thin-films," Nat. Commun. **2**, 518 (2011).
[33]A. J. Lee *et al.*, "Metallic ferromagnetic films with magnetic damping under 1.4×10^{-3}," Nat. Commun. **8**, 234 (2017).
[34]S. Kim, "Ultrafast magneto-optical measurements for probing magnon–phonon interactions in nanomagnets," Nat. Rev. Phys. **4**, 288 (2022).
[35]L. Dreher *et al.*, "Surface acoustic wave driven ferromagnetic resonance in nickel thin films: Theory and experiment," Phys. Rev. B **86**, 134415 (2012).
[36]S. Kim and H. Schmidt, "Magnetoelastic control of nanomagnet dynamics," in *Nanomagnets as Dynamical Systems*, edited by S. Bandyopadhyay and A. Barman (Springer Nature Switzerland, Cham, 2024), pp. 97–142.
[37]A. Imamoğlu, "Cavity QED based on collective magnetic dipole coupling: Spin ensembles as hybrid two-level systems," Phys. Rev. Lett. **102**, 083602 (2009).
[38]S. Zhuang *et al.*, "Hybrid magnon-phonon cavity for large-amplitude terahertz spin-wave excitation," Phys. Rev. Appl. **21**, 044009 (2024).